



UNIVERSITY OF LEEDS

This is a repository copy of *Sensitivity Ellipsoids for Force Control of Magnetic Robots With Localization Uncertainty*.

White Rose Research Online URL for this paper:
<http://eprints.whiterose.ac.uk/147091/>

Version: Accepted Version

Article:

Slawinski, PR, Simaan, N, Taddese, AZ et al. (2 more authors) (2019) Sensitivity Ellipsoids for Force Control of Magnetic Robots With Localization Uncertainty. *IEEE Transactions on Robotics*, 35 (5). pp. 1123-1135. ISSN 1552-3098

<https://doi.org/10.1109/TRO.2019.2917817>

© 2019 IEEE. This is an author produced version of a paper published in *IEEE Transactions on Robotics*. Personal use of this material is permitted. Permission from IEEE must be obtained for all other uses, in any current or future media, including reprinting/republishing this material for advertising or promotional purposes, creating new collective works, for resale or redistribution to servers or lists, or reuse of any copyrighted component of this work in other works. Uploaded in accordance with the publisher's self-archiving policy.

Reuse

Items deposited in White Rose Research Online are protected by copyright, with all rights reserved unless indicated otherwise. They may be downloaded and/or printed for private study, or other acts as permitted by national copyright laws. The publisher or other rights holders may allow further reproduction and re-use of the full text version. This is indicated by the licence information on the White Rose Research Online record for the item.

Takedown

If you consider content in White Rose Research Online to be in breach of UK law, please notify us by emailing eprints@whiterose.ac.uk including the URL of the record and the reason for the withdrawal request.



eprints@whiterose.ac.uk
<https://eprints.whiterose.ac.uk/>

Sensitivity Ellipsoids for Force Control of Magnetic Robots with Localization Uncertainty

Piotr R. Slawinski¹, *Student Member, IEEE*, Nabil Simaan¹, *Senior Member, IEEE*,
Addisu Z. Taddese¹, Keith L. Obstein^{1,2}, Pietro Valdastris³, *Senior Member, IEEE*

Abstract—The navigation of magnetic medical robots typically relies on localizing an actuated, intracorporeal, ferromagnetic body and back-computing a necessary field and gradient that would result in a desired wrench on the device. Uncertainty in this localization degrades the precision of force transmission. Reducing applied force uncertainty may enhance tasks such as *in-vivo* navigation of miniature robots, actuation of magnetically guided catheters, tissue palpation, as well as simply ensuring a bound on forces applied on sensitive tissue. In this paper, we analyzed the effects of localization noise on force uncertainty by using sensitivity ellipsoids of the magnetic force Jacobian and introduced an algorithm for uncertainty reduction. We validated the algorithm in both a simulation study and in a physical experiment. In simulation, we observed reductions in estimated force uncertainty by factors of up to 2.8 and 3.1 when using one and two actuating magnets, respectively. On a physical platform, we demonstrated a force uncertainty reduction by a factor of up to 2.5 as measured using an external sensor. Being the first consideration of force uncertainty resulting from noisy localization, this work provides a strategy for investigators to minimize uncertainty in magnetic force transmission.

Index Terms—force control, localization, magnetic actuation, medical robots and systems

I. INTRODUCTION

MAGNETIC actuation for use in medicine has been investigated since 1842 with the first use of computer guidance occurring in the late 1980s [1]. The use of magnetic actuation to manipulate a ferromagnetic body via an extracorporeal field offers advantages in terms of invasiveness and miniaturization; thereby eliminating the need for on-board actuation mechanisms and motion-dedicated power. It has been

widely applied for medical applications including drug delivery, nano- micro- and meso- scale navigation, the actuation of continuum robots and needles, ablation, diagnostics, tissue penetration, and the actuation of laparoscopic devices [2]–[6].

The control of magnetic devices is implemented by imparting a field misalignment and gradient on the driven magnet which induces a wrench. The computation of this field and its gradient results in closed-loop magnetic control which has been developed previously by estimating the device state, e.g. localizing it, and using magnetic field models to compute necessary fields and gradients for motion [7]–[9]. Another approach for closed-loop control that was recently developed relies on estimating the relationship between the actuating field and device motion directly [10]. This method bypasses the need for localizing an actuated device; however, it cannot be applied in systems where magnetic wrench estimation or absolute positioning is desired. Methods that have been investigated for obtaining feedback of the position, and/or orientation, of intracorporeal actuated devices include:

- 1) visual feedback [11];
- 2) microwave imaging [12];
- 3) radio-frequency localization [13];
- 4) ultrasound [14];
- 5) positron emission tomography [15];
- 6) magnetic localization [9], [16]–[18];

This paper is motivated by the lack of investigation into the effects of localization uncertainty on magnetic force transmission. Regardless of the localization method used, location uncertainty, or noise, introduces a disturbance in the applied magnetic wrench and thus negatively effects position and force control accuracy and robustness. Similar uncertainty effects have been extensively investigated in mechanical linkage architectures, but little consideration exists in the realm of magnetic actuation [19]–[21]. Localization uncertainty, as it pertains to the task of magnetic force transmission, has not been investigated. Furthermore, a framework for considering such uncertainty has not been developed.

A prior study concerning uncertainty in magnetic actuation was conducted on a system consisting of a single permanent magnet that rotated to generate a rotating magnetic field. To avoid unexpected behavior and loss of control of a rotating robot, the authors characterized the effects of error in the chosen applied field rotation axis, field magnitude, and instantaneous rotational velocity while attributing worst-case bounds [22]. The distinction between rotating and non-rotating device control is significant as the mechanics of actuation

Manuscript received February 11, 2019; accepted May 13, 2019. This work was supported by the National Institute of Biomedical Imaging and Bioengineering, USA of the National Institutes of Health under Award no. R01EB018992, by the National Science Foundation Graduate Research Fellowship Program under Grant 1445197, by the European Research Council under Award no. 818045, by the Royal Society, U.K., by the Engineering and Physical Sciences Research Council, U.K., under Awards no. EP/P027938/1 and EP/R045291/1, and by the Italian Ministry of Health funding programme Ricerca Sanitaria Finalizzata 2013 - Giovani Ricercatori project n. PE-2013-02359172. This paper was recommended for publication by Associate Editor J. Abbott and Editor P. Dupont upon evaluation of the reviewers' comments (*Corresponding author: Piotr R. Slawinski*)

¹P.R. Slawinski, N. Simaan, A.Z. Taddese, and K.L. Obstein are from the Department of Mechanical Engineering, Vanderbilt University, Nashville, TN, USA (e-mail: piotr.r.slawinski@gmail.com; nabil.simaan@vanderbilt.edu; addisu@taddese.com; keith.obstein@vumc.org)

²K.L. Obstein is from the Division of Gastroenterology, Vanderbilt University Medical Center, Nashville, TN, USA

³P. Valdastris is from the Institute of Robotics, Autonomous Systems and Sensing, School of Electronic and Electrical Engineering, University of Leeds, Leeds, UK (e-mail: p.valdastris@leeds.ac.uk)

are different: a rotating robot is typically propelled via the mechanics of threading through a medium, whereas a non-rotating robot is simply subject to applied forces and torques and dynamically reacts to them.

The primary contributions of this work are (1) the proposition of a method for characterizing the effects of localization noise on uncertainty in the applied magnetic force on an actuated intracorporeal magnet and (2) the application of this characterization to a force control task where one desires to reduce force uncertainty in a chosen direction. We use sensitivity ellipsoids [23] to characterize the mapping between localization noise and the uncertainty in applied force. We use force ellipsoids in this analysis and note that magnetic actuation is unique with respect to typical rigid-link manipulators in that a duality between joint and task manipulability does not exist, as the only motion of the robot results from an applied wrench. We have demonstrated that actuation redundancy in a magnetic system can be utilized to adjust the shape of force sensitivity ellipsoids that, in turn, results in a force control that has a lower uncertainty in a direction of choice. This methodology is valid for magnetic actuation systems with one or more actuating permanent magnets. The approach we present can be expanded for systems of electromagnets by replacing EM twist relations with current inputs, or combining the two in the case of mobile electromagnet systems [24].

We begin by summarizing our magnetic modeling technique in Section II. In Section II-C, we discuss the implication of sensitivity ellipsoids and demonstrate how the actuation workspace can be analyzed. In section III, we propose an algorithm for using sensitivity ellipsoid information in a force control task and demonstrate the algorithm's function both in simulation (Section IV-B) and on our experimental platform (Section IV-C). Finally, we summarize our work and discuss its implications in Sections V and VI.

II. MODELING OF MAGNETIC FORCE UNCERTAINTY

A. Assumptions

In this work, we will make use of five assumptions related to the magnetic field, the motion of the actuated intracorporeal magnet (IM), and the localization of the actuating, extracorporeal, magnet (EM). First, we will assume that the magnets can be modelled as ideal dipoles; this is an appropriate approximation as a permanent magnet with identical length and diameter, as we use in our system, has been shown to resemble a dipole field with approximately 1% error at one normalized distance from the EM's center (10 cm in our case) [25]. Second, we assume that slow motions of the IM which simplifies the mathematical formulations. This assumption has been used in our previous works with success [26]. Third, we assume ideal knowledge, *i.e.* no uncertainty, of the configuration of the EM. In this work, the EM is fixed at the end-effector of a serial industrial manipulator and the configuration of the EM is computing using direct kinematics. The assumption of ideal EM configuration knowledge is valid as the kinematics of the rigid-link manipulator are likely to have a significantly higher accuracy than magnetic localization

TABLE I
NOMENCLATURE

Symbol	Description
\mathbf{v}	Vector (lowercase, bold)
\mathbf{M}	Matrix (uppercase)
\mathbf{I}	Identity matrix
\mathbf{J}	Jacobian matrix
$\tilde{\mathbf{J}}$	Jacobian matrix written in terms of differential rotation
δ	Infinitesimal change
$\hat{\mathbf{v}}$	Unit vector
\mathbf{p}_{e_k}	Position of k^{th} EM in inertial frame $\in \mathbb{R}^3$
\mathbf{p}_i	Position of IM in inertial frame $\in \mathbb{R}^3$
$\mathbf{p}_k = \mathbf{p}_i - \mathbf{p}_{e_k}$	Relative position vector from k^{th} EM to IM $\in \mathbb{R}^3$
$\hat{\mathbf{m}}_{e_k}$	Magnetic moment vector of k^{th} EM $\in \mathbb{R}^3$
$\hat{\mathbf{m}}_i$	Magnetic moment vector of IM $\in \mathbb{R}^3$
$\mathbf{x}_e = [\mathbf{p}_e; \hat{\mathbf{m}}_e]$	Pose of EM $\in \mathbb{R}^6$
$\mathbf{x}_i = [\mathbf{p}_i; \hat{\mathbf{m}}_i]$	Pose of IM $\in \mathbb{R}^6$
$\mathbf{x}_d = [\mathbf{p}_d; \hat{\mathbf{m}}_d]$	IM pose disturbance from localization uncertainty $\in \mathbb{R}^6$

systems. Fourth, we assume Jacobian linearity to be always valid. This assumption is discussed in a latter portion of this section, however, it is a safe assumption as our controller runs at over 50 Hz. Fifth, we assume that the Jacobian used for magnetic actuation is not affected by localization noise. We show that our results suggest this to be an acceptable assumption owing to our high control rate.

B. Error Propagation in Magnetic Coupling

The point-dipole model describes the field of a particle and can be used to approximate the fields of permanent magnets of various shape [25]. In this section, we briefly summarize the model for the purpose of understanding control relations, and present linearizations that are used in sensitivity analysis and control.

The discussion, methodology, and experiments in this document serve as a case study for our approach to sensitivity analysis and optimization. We present the methodology for a system of one or more EMs that actuate, via imparted wrenches, a single IM. The gradient and direction of the magnetic field at the IM is controlled by imparting twists on the EM(s). We distinguish references to the magnets by using an "e" subscript to reference EMs and an "i" subscript to refer to the IM. In the event that multiple EMs are used, an additional enumeration subscript "k" is applied. The nomenclature used in this document is shown in Table I, with some parameters visualized in Fig. 1 where a planar dipole field shape is shown for reference.

The magnetic field of a single EM applied at an IM can be expressed via Eq. (1) whereas, owing to magnetic fields being vector fields, the total field at an IM can be expressed via Eq. (2) [27].

$$\mathbf{b}_{e_k}(\mathbf{p}_k) = \frac{\mu_0}{4\pi \|\mathbf{p}_k\|^3} (3\hat{\mathbf{p}}_k \hat{\mathbf{p}}_k^T \mathbf{m}_{e_k} - \mathbf{m}_{e_k}) \quad (1)$$

$$\mathbf{b}_e = \sum_{j=1}^n \mathbf{b}_{e_j}(\mathbf{p}_j) \quad (2)$$

The magnetic wrench induced on the IM by external fields

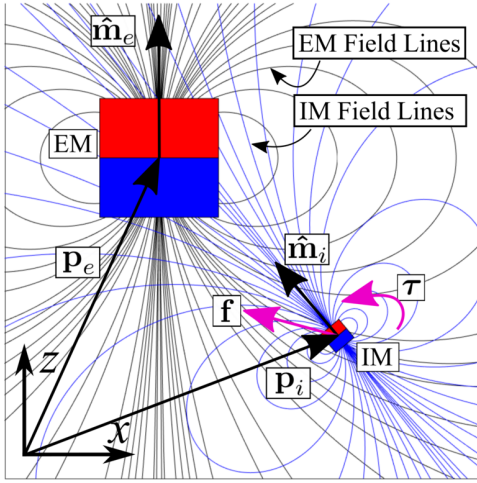


Fig. 1. Nomenclature of magnets and visual representation of the dipole fields of an IM and EM, without superposition, as well as the force and torque that are imparted on the IM by the EM.

can be expressed via Eq. (3) and Eq. (4) [7].

$$\mathbf{f} = (\mathbf{m}_i \cdot \nabla) \mathbf{b}_e = \sum_{j=1}^n \left(\frac{3\mu_0 \|\mathbf{m}_{e_j}\| \|\mathbf{m}_i\|}{4\pi \|\mathbf{p}_j\|^4} (\hat{\mathbf{m}}_{e_j} \hat{\mathbf{m}}_i^T + \hat{\mathbf{m}}_i \mathbf{m}_{e_j}^T + (\hat{\mathbf{m}}_i^T (\mathbf{I} - 5\hat{\mathbf{p}}_j \hat{\mathbf{p}}_j^T) \hat{\mathbf{m}}_{e_j}) \mathbf{I}) \right) \hat{\mathbf{p}} \quad (3)$$

$$\begin{aligned} \boldsymbol{\tau} &= \mathbf{m}_i \times \mathbf{b}_e \\ &= \sum_{j=1}^n \left(\frac{\mu_0 \|\mathbf{m}_{e_j}\| \|\mathbf{m}_i\|}{4\pi \|\mathbf{p}_j\|^3} \hat{\mathbf{m}}_i \times (3\hat{\mathbf{p}}_j \hat{\mathbf{p}}_j^T - \mathbf{I}) \hat{\mathbf{m}}_{e_j} \right) \end{aligned} \quad (4)$$

The linearization that relates infinitesimal EM motion and the change in wrench, $\delta \mathbf{w}$, applied on the IM can be evaluated either numerically or analytically. An analytical formulation of Jacobians that relates the motion of a single EM to changes in magnetic force on the IM and heading of the IM was developed by Mahoney and Abbott [7] and later expanded by Taddese *et al.* [28] to include consideration for magnetic torque in cases where alignment of the IM to the external field should not be assumed. This expression is shown in Eq. (5). We separate EM and IM terms in Eq. (6), and expand the expression for cases of actuation via multiple EMs in Eq. (7). We refer the reader to [28] for explicit definitions of differential terms.

$$\delta \mathbf{w}_k = \begin{bmatrix} \delta \mathbf{f}_k \\ \delta \boldsymbol{\tau}_k \end{bmatrix} = \begin{bmatrix} \frac{\partial \mathbf{f}_k}{\partial \mathbf{p}_k} & \frac{\partial \mathbf{f}_k}{\partial \hat{\mathbf{m}}_{e_k}} & \frac{\partial \mathbf{f}_k}{\partial \hat{\mathbf{m}}_i} \\ \frac{\partial \boldsymbol{\tau}_k}{\partial \mathbf{p}_k} & \frac{\partial \boldsymbol{\tau}_k}{\partial \hat{\mathbf{m}}_{e_k}} & \frac{\partial \boldsymbol{\tau}_k}{\partial \hat{\mathbf{m}}_i} \end{bmatrix} \begin{bmatrix} \delta \mathbf{p}_k \\ \delta \hat{\mathbf{m}}_{e_k} \\ \delta \hat{\mathbf{m}}_i \end{bmatrix} \quad (5)$$

$$\begin{aligned} \begin{bmatrix} \delta \mathbf{f}_k \\ \delta \boldsymbol{\tau}_k \end{bmatrix} &= \begin{bmatrix} \frac{\partial \mathbf{f}_k}{\partial \mathbf{p}_{e_k}} & \frac{\partial \mathbf{f}_k}{\partial \hat{\mathbf{m}}_{e_k}} \\ \frac{\partial \boldsymbol{\tau}_k}{\partial \mathbf{p}_{e_k}} & \frac{\partial \boldsymbol{\tau}_k}{\partial \hat{\mathbf{m}}_{e_k}} \end{bmatrix} \begin{bmatrix} \delta \mathbf{p}_{e_k} \\ \delta \hat{\mathbf{m}}_{e_k} \end{bmatrix} + \begin{bmatrix} \frac{\partial \mathbf{f}_k}{\partial \mathbf{p}_i} & \frac{\partial \mathbf{f}_k}{\partial \hat{\mathbf{m}}_i} \\ \frac{\partial \boldsymbol{\tau}_k}{\partial \mathbf{p}_i} & \frac{\partial \boldsymbol{\tau}_k}{\partial \hat{\mathbf{m}}_i} \end{bmatrix} \begin{bmatrix} \delta \mathbf{p}_i \\ \delta \hat{\mathbf{m}}_i \end{bmatrix} \\ &= \mathbf{J}_{e_k} \begin{bmatrix} \delta \mathbf{p}_{e_k} \\ \delta \hat{\mathbf{m}}_{e_k} \end{bmatrix} + \begin{bmatrix} \frac{\partial \mathbf{f}_k}{\partial \mathbf{p}_i} & \frac{\partial \mathbf{f}_k}{\partial \hat{\mathbf{m}}_i} \\ \frac{\partial \boldsymbol{\tau}_k}{\partial \mathbf{p}_i} & \frac{\partial \boldsymbol{\tau}_k}{\partial \hat{\mathbf{m}}_i} \end{bmatrix} \begin{bmatrix} \mathbf{I} & \mathbf{0} \\ \mathbf{0} & \mathbf{S}(\hat{\mathbf{m}}_i)^T \end{bmatrix} \begin{bmatrix} \delta \mathbf{p}_i \\ \boldsymbol{\omega}_i \end{bmatrix} \\ &= \mathbf{J}_{e_k} \begin{bmatrix} \delta \mathbf{p}_{e_k} \\ \delta \hat{\mathbf{m}}_{e_k} \end{bmatrix} + \begin{bmatrix} \mathbf{J}_{F p_i} & \tilde{\mathbf{J}}_{F \boldsymbol{\omega}_i} \\ \mathbf{J}_{T p_i} & \tilde{\mathbf{J}}_{T \boldsymbol{\omega}_i} \end{bmatrix} \begin{bmatrix} \delta \mathbf{p}_i \\ \boldsymbol{\omega}_i \end{bmatrix} \\ &= \mathbf{J}_{e_k} \begin{bmatrix} \delta \mathbf{p}_{e_k} \\ \delta \hat{\mathbf{m}}_{e_k} \end{bmatrix} + \tilde{\mathbf{J}}_{i_k} \begin{bmatrix} \delta \mathbf{p}_i \\ \boldsymbol{\omega}_i \end{bmatrix} \end{aligned} \quad (6)$$

Here, $\mathbf{S}(\mathbf{a}) \in so(3)$ denotes the skew-symmetric form of the cross-product operation. In $\tilde{\mathbf{J}}_i$ of Eq. (6), we use partial derivatives with respect to differential rotation ($\boldsymbol{\omega}_i$), rather than dipole heading, as angular velocity is the mode of localization feedback. In Eq. (7) we expand Eq. (6) to account for multiple EMs used for actuation.

$$\begin{aligned} \delta \mathbf{w} &= \delta \mathbf{w}_e + \delta \mathbf{w}_i \\ \begin{bmatrix} \delta \mathbf{f} \\ \delta \boldsymbol{\tau} \end{bmatrix} &= \mathbf{J}_e \begin{bmatrix} \delta \mathbf{p}_e \\ \delta \hat{\mathbf{m}}_e \end{bmatrix} + \tilde{\mathbf{J}}_i \begin{bmatrix} \delta \mathbf{p}_i \\ \boldsymbol{\omega}_i \end{bmatrix} \\ \delta \mathbf{w} &= \begin{bmatrix} \mathbf{J}_{F e} \\ \mathbf{J}_{T e} \end{bmatrix} \delta \mathbf{x}_e + \begin{bmatrix} \tilde{\mathbf{J}}_{F i} \\ \tilde{\mathbf{J}}_{T i} \end{bmatrix} \begin{bmatrix} \delta \mathbf{p}_i \\ \boldsymbol{\omega}_i \end{bmatrix} \\ &= \begin{bmatrix} \mathbf{J}_{F e_1} & \dots & \mathbf{J}_{F e_k} \\ \mathbf{J}_{T e_1} & \dots & \mathbf{J}_{T e_k} \end{bmatrix} [\delta \mathbf{x}_{e_1}; \dots; \delta \mathbf{x}_{e_k}]^T + \\ &\quad \dots \left(\sum_{i=1}^n \begin{bmatrix} \tilde{\mathbf{J}}_{F i_k} \\ \tilde{\mathbf{J}}_{T i_k} \end{bmatrix} \right) \begin{bmatrix} \delta \mathbf{p}_i \\ \boldsymbol{\omega}_i \end{bmatrix} \end{aligned} \quad (7)$$

We now have a full expression for applied wrench of $\delta \mathbf{w}$ in Eq. (7) which we interpret as: the infinitesimal change in wrench applied on the IM by the EM(s) results from the change in pose of the EM(s) and IM. It should be noted that the influences of Jacobians $\mathbf{J}_{F e_k}$ and $\tilde{\mathbf{J}}_{F i}$ are nearly identical if a single EM is used. The relative impact of $\tilde{\mathbf{J}}_{F i}$ decreases as more EMs are used and has approximately 60% of the influence of $\mathbf{J}_{F e_k}$ when two EMs are used. As $\delta \mathbf{w}_i$ is null owing to an assumption of slow IM motion, we replace it with an algorithmic wrench disturbance term to account for the effects of localization uncertainty in a force application task. This new term can be interpreted as a numerical uncertainty in wrench that does not exist in the physical world, but is perceived by the controller. With this disturbance wrench, our expression for the change in applied wrench becomes $\delta \mathbf{w} = \delta \mathbf{w}_e + \delta \mathbf{w}_d$. We will model $\delta \mathbf{w}_d$ the same way as $\delta \mathbf{w}_i$ *i.e.* we use the Jacobian $\tilde{\mathbf{J}}_i$ and refer to the disturbance twist as $\delta \mathbf{x}_d$. Hereafter, we use $\mathbf{J}_e \in \mathbb{R}^{6 \times 6k}$ for actuation and $\tilde{\mathbf{J}}_i \in \mathbb{R}^{6 \times 6}$ for analyzing the mapping of localization noise to a disturbance wrench. Whereas ideal knowledge of EM positioning is assumed here, Eq. (7) should be augmented in the event that a larger uncertainty exists in the configuration of the EM.

The expression in Eq. (7) remains valid as long as the linearity assumption holds; *i.e.* linear and angular perturbations of IM pose are small enough. To evaluate an approximate linearity range, we conducted a numerical simulation using 90,000 configurations of an IM and EM, where the IM was spanned to be between 14 and 16 cm from the EM, and found the linearity range to be 14.3 mm and 6.1°. The conditions for linearity in magnetic force were as follows: the error magnitude of the linearized force less than or equal to 10%, and the direction error between the linearized force and nonlinear truth is less than or equal to 10°. We note that the aforementioned angular range of 6.1° refers to rotation of the IM, while the angular error of linearized force refers to an angle between resultant force vectors. Furthermore, we note that we assume $\mathbf{J}_{F e_k}$ to be unaffected by localization noise. The implication of this noise is a deviation of commanded magnet motion from the optimal, *i.e.* the direction that reduces force

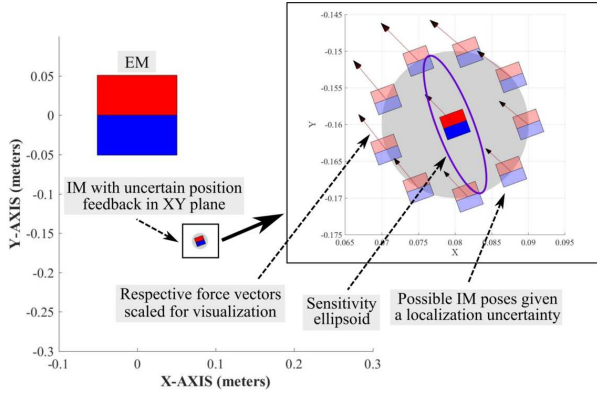


Fig. 2. Graphical representation of a single EM that actuates an IM, possible uncertain poses of the IM when zoomed in, and the sensitivity ellipsoid that relates position uncertainty with uncertainty in applied force. Both force and motion are considered only in the XY plane for visualization.

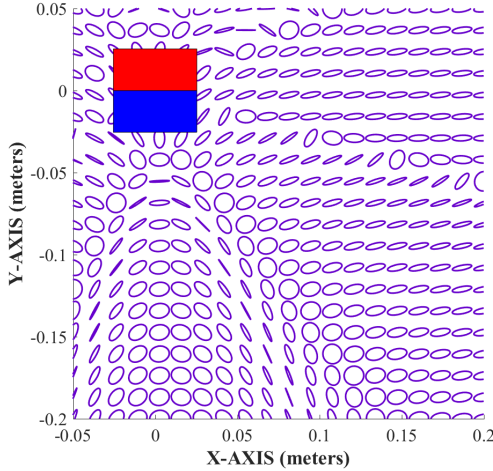


Fig. 3. A planar representation of shape variation of the $\partial \mathbf{f} / \partial \mathbf{p}_i$ Jacobian sensitivity ellipsoid. The IM orientation is kept constant while it is translated throughout this planar workspace in a set of discrete points where the ellipsoids are shown. All ellipsoids are normalized in scale for visualization.

error. This assumption degrades as the rate of control decreases and the resultant effect is a non-smooth motion of the EM(s).

C. Analysis of Force Uncertainty Using Sensitivity Ellipsoids

To characterize the effect of localization uncertainty, we study $\tilde{\mathbf{J}}_i$, a linear mapping between infinitesimal changes in IM pose and uncertainty in applied wrench. An instantaneous visualization of the Jacobian mapping, a sensitivity ellipsoid, has been frequently used in rigid-link robotics for considering losses in degrees-of-freedom (DoFs), kinematic and dynamic manipulability, and sensitivity, but has not before been utilized in magnetic control. For derivations of ellipsoid usage we refer the reader to texts by Yoshikawa and Nakamura [23], [29] as they will be omitted here for brevity apart from relations that are necessary for understanding the topic at hand. The force uncertainty that results from localization noise is dictated by $\tilde{\mathbf{J}}_{Fi}$ which maps infinitesimal IM twist to a change in force applied on the IM.

The mapping of $\tilde{\mathbf{J}}_{Fi}$ can be visualized by considering a set of unit inputs of $\delta \mathbf{x}_d$ uniformly distributed such as to resemble a unit sphere. The set of mapped force vectors is defined by the hyper-ellipsoid:

$$\delta \mathbf{f}_d^T (\tilde{\mathbf{J}}_{Fi} \tilde{\mathbf{J}}_{Fi}^T)^{-1} \delta \mathbf{f}_d = 1 \quad (8)$$

The major and minor axes of this hyper-ellipsoid constitute the directions of maximum and minimum wrench uncertainty, respectively. The mapping can be explicitly characterized using singular value decomposition. We consider the decomposition of $\tilde{\mathbf{J}}_{Fi}$ to be $\mathbf{U}\Sigma\mathbf{V}^T$ where \mathbf{U} and \mathbf{V} are two orthonormal spaces where the columns of \mathbf{U} are called left-singular vectors and the columns of \mathbf{V} are called right-singular vectors. The diagonal of Σ contains the singular values, s_i , of $\tilde{\mathbf{J}}_{Fi}$ which are arranged such that $s_1 > s_2 > s_3$. Conceptually, the left-singular vectors indicate the principal directions of infinitesimal wrench application whereas the right-singular vectors indicate the corresponding directions of infinitesimal twists that cause the respective wrenches. Thus, the longer that a sensitivity ellipsoid is in a particular direction, the more uncertain the applied wrench is. In a force control task, we desire for this ellipsoid to be as small as possible in the direction that force is to be controlled with the most certainty. A 2D conceptual representation of a sensitivity ellipsoid, developed via the dipole model, is shown in Fig. 2. The shape of the ellipsoids may vary significantly throughout an EM's workspace as demonstrated in Fig. 3; here, a constant orientation of an IM is chosen and the dipole ellipsoids are plotted at a discrete set of IM positions on a plane. As the accuracy of the dipole model of the EM increases with distance, so does the accuracy of the sensitivity ellipsoids.

We aim to reduce the uncertainty in a force application task, such as applying a contact force, in a direction of interest that we will hereafter refer to as $\hat{\mathbf{c}}$, where ‘‘c’’ denotes ‘‘contact’’. This inherently results in a desired task of reducing the spatial derivative of force in the direction of contact. We wish to identify the size of the mapping of Jacobian $\tilde{\mathbf{J}}_{Fi}$ in the direction of $\hat{\mathbf{c}}$. To do so, we compute the volume of the sensitivity ellipsoid of $\tilde{\mathbf{J}}_{Fi}$ projected in the direction of $\hat{\mathbf{c}}$ via projection matrix $\mathbf{P}_c = \hat{\mathbf{c}}\hat{\mathbf{c}}^T$. We hereafter refer to the ellipsoid length of $\tilde{\mathbf{J}}_{Fi}$ in the direction of $\hat{\mathbf{c}}$ via the scalar g . The definition of g is shown in Eq. (9) whereas the expression for computing the volume of a hyper-ellipsoid, as defined in [29], is shown in Eq. (10) where $\Gamma(\star)$ is the gamma function and m is the length of the hyper-ellipsoid. We note that the $vol()$ function of Eq. (10) computes the product of non-zero singular values; this facilitates not only the computation of volume, but also area, or length, in the case of the Jacobian being rank deficient. We refer to the magnetic force whose uncertainty we wish to minimize as $f_c = \mathbf{f} \cdot \hat{\mathbf{c}}$ and refer to this as the ‘‘contact force’’. The force f_c is the force that is exerted on the environment by the IM. The parameters of a sensitivity ellipsoid are visualized in Fig. 4.

$$g \equiv vol(\mathbf{P}_c \tilde{\mathbf{J}}_{Fi}) \quad (9)$$

$$vol(\mathbf{J}) = \frac{\pi^{m/2}}{\Gamma(1 + m/2)} \prod_{i=1}^j \sigma_i \quad (10)$$

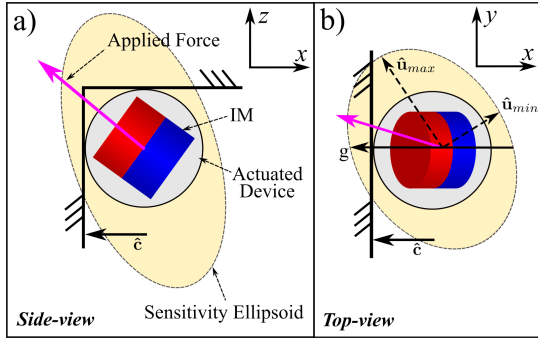


Fig. 4. Conceptual schematic of a force sensitivity ellipsoid. The ellipsoid view represents a plane-cut through the ellipsoid, which would be achieved by projecting a Jacobian. Sub-figure a) shows a side view of ellipsoid, whereas sub-figure b) shows the top view of ellipsoid. In the top view, we show the non-circular projection where g takes on a value between the magnitudes of the ellipsoid length in the \hat{u}_{min} and \hat{u}_{max} direction.

Localization feedback with noise will result in an uncertain estimated force as mapped by the nonlinear Eq. (3). We refer to this mapped wrench hereafter as f_{c_a} where the subscript “a” is used to denote that this is the contact force as interpreted by an algorithm. We note that the difference between f_c and f_{c_a} is that f_c is a true force that is exerted on the environment, whereas f_{c_a} is the force as perceived by a control algorithm. The value of f_c can be more precisely controlled when the uncertainty of f_{c_a} is minimized. We quantify force uncertainty using coefficients of variation CV_a and CV_t which represent the algorithmic contact force uncertainty, Eq. (11), and the true contact force uncertainty, Eq. (12), respectively. Here, *STD* indicates the standard deviation.

$$CV_a = 100 \times \left| \frac{STD(f_{c_a})}{MEAN(f_{c_a})} \right| \quad (11)$$

$$CV_t = 100 \times \left| \frac{STD(f_c)}{MEAN(f_c)} \right| \quad (12)$$

To visualize the relationship between these values in the presence of localization noise, we conducted a set of 5000 numerical simulations where a uniform localization noise of 15 mm and 15° was applied with a single stationary EM and a stationary IM. This linear noise translates to approximately 135% of the size (11.11 mm diameter and length) of the IM used in our previous experimental work [9], [26]. In each of the 5000 simulations, the EM’s pose was randomly chosen within a distance between magnets of 15 cm with a STD of 1 cm, or in a bound of approximately 7% of the separating distance. The position of the EM around the IM was chosen by a uniform random distribution of relative position vectors \mathbf{p} . Similarly, the heading of the EM was chosen randomly as well. For each pose of the EM, 1000 mappings from uncertain localization to f_{c_a} were computed. Noise was assumed to have a Gaussian distribution. We note that the nonlinear force mapping was applied here. From this, we computed the relationships between g and the STD of $|f_{c_a}|$, Fig. 5, as well as between $mean(g)/mean(|f_{c_a}|)$ and CV_a , Fig. 6. We note that $mean(g)/mean(|f_{c_a}|)$ is not equal to $mean(g)/|f_{c_a}|$. We do not directly plot the relationship between g and CV_a as the latter is normalized with the contact force magnitude. We

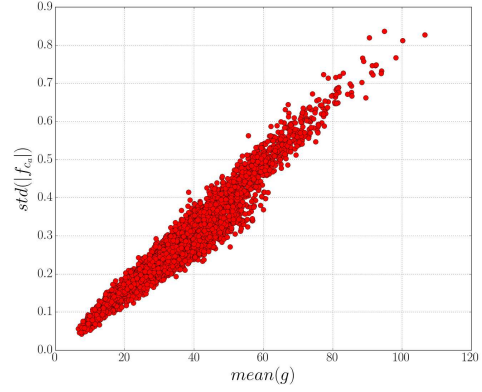


Fig. 5. Numerical simulation result that shows the relationship between the STD of f_{c_a} , which is the contact force as estimated by the system, and the mean value of g . Here, the mean refers to the mean value of the 1000 data points of each of the 5000 simulation.

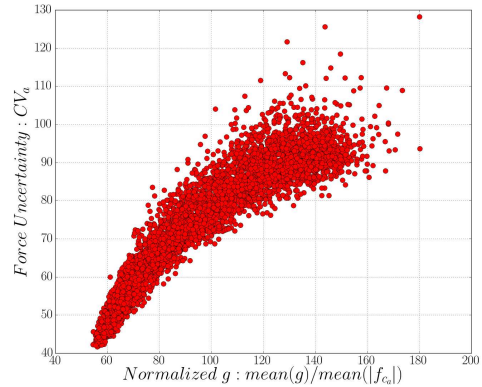


Fig. 6. Numerical simulation result that shows the relationship between the mean normalized value of g and CV_a . Here, the mean refers to the mean value of the 1000 data points of each of the 5000 simulation.

found that g and the STD of $|f_{c_a}|$ are related linearly with a coefficient of determination of 0.94, whereas the relation between $g/|f_{c_a}|$ and CV_a has a coefficient of determination of 0.87. As the results in Fig. 6 are normalized with force magnitude, a nonlinearity is introduced that results from the relation shown in Eq. (3). We conclude that reducing g will result in a reduction in uncertainty

The uncertainty of f_{c_a} , the contact force as estimated by the system, is directly affected by the value of g and thus, since g can be controlled by the actuating field, the uncertainty of f_{c_a} can also be controlled. The uncertainty in the true force on the environment, f_c , however, is dependent not only on the estimate f_{c_a} , but also on environmental factors, and thus cannot directly be controlled. We proceed with an assumption that if the estimated contact force has a lower uncertainty, then the true contact force will likely have a lower uncertainty as well.

III. FORCE CONTROL

To implement magnetic control, we wish to determine which EM motions will result in desired wrenches on the IM that,

in turn, will act on the IM and result in desired force and/or motion. The motion of an IM is dictated by device mechanics and dynamics, as well as environmental interactions. Rather than precisely modeling environmental effects which may be cumbersome, prior works have successfully implemented closed-loop control without environmental modelling [7], [9], [26] which we have done in this work as well. To choose a desired EM motion, a desired infinitesimal change in force must be determined, which we refer to as $\delta \mathbf{f}_{des}$. Given that this is a 3 DoF actuation task, and the actuation system has 5 DoFs, \mathbf{J}_{Fe} contains 2 DoFs of redundancy, which we use here for sensitivity minimization. The action of the controller is dependent on the method of inversion of the \mathbf{J}_{Fe} Jacobian. One acceptable inversion method is to use a weighted right pseudo-inverse as shown in Eq. (13) [30]. This inversion is a constrained linear optimization that minimizes the objective function $\delta \mathbf{x}_e^T \mathbf{W} \delta \mathbf{x}_e$ where \mathbf{W} is a diagonal weight matrix whose diagonal weights can be chosen such that certain values of $\delta \mathbf{x}_e$ are minimized with preference. The weight matrix \mathbf{W} can be used for performance tuning as the vector $\delta \mathbf{x}_e$ contains terms of various units; an example result of weight tuning could be a preference for EM rotation rather than translation. In implementations in this paper, \mathbf{W} was set to an identity matrix.

$$\delta \mathbf{x}_e = \mathbf{W}^{-1} \mathbf{J}_{Fe}^T (\mathbf{J}_{Fe} \mathbf{W}^{-1} \mathbf{J}_{Fe}^T)^{-1} \delta \mathbf{f}_{des} = \mathbf{J}_{Fe}^{\#} \delta \mathbf{f}_{des} \quad (13)$$

To reduce uncertainty in \mathbf{f}_e , we aim to reduce the value of g . In this section we present a control method that reduces the value of g using a gradient projection method [31] in magnetic control. Here, we alter the shape of the sensitivity ellipsoid using EM DoFs that are redundant for completing the desired task of 3 DoF force control. We thus augment the control strategy of Eq. (13) to Eq. (14) where the scalar value β is a user defined constant that, when set to a negative value, projects the gradient onto the null space of \mathbf{J}_{Fe} as to minimize an objective function. The value of $\delta \mathbf{f}_{des}$ is task dependent and will be specified in reference to experiments later in this manuscript. The gradient of g is computed via Eq. (15) where a gradient with respect to a single EM motion is computed. This same method is utilized by stacking gradients if more than one EM is used. We compute the gradient numerically using Python and have observed a computation time between 2 and 4 ms when using a single EM. In our implementation, we normalized the gradient and capped the impact of the homogeneous solution.

$$\begin{aligned} \delta \mathbf{x}_e &= \delta \mathbf{x}_{e_{particular}} + \delta \mathbf{x}_{e_{homogeneous}} = \delta \mathbf{x}_{e_p} + \delta \mathbf{x}_{e_h} \\ &= \mathbf{J}_{Fe}^{\#} \delta \mathbf{f}_{des} + \beta (\mathbf{I} - \mathbf{J}_{Fe}^{\#} \mathbf{J}_{Fe}) \nabla_{\mathbf{x}_e} g(\mathbf{x}_e, \mathbf{x}_i) \end{aligned} \quad (14)$$

$$\nabla_{\mathbf{x}_e} g = \begin{bmatrix} \frac{\partial \text{vol}(\mathbf{P}_c \mathbf{J}_{Fi})}{\partial \mathbf{p}_e} \\ \frac{\partial \text{vol}(\mathbf{P}_c \mathbf{J}_{Fi})}{\partial \hat{\mathbf{m}}_e} \end{bmatrix} \quad (15)$$

IV. EXPERIMENTAL VALIDATION

A. Experimental Setup

We conducted experiments in both a simulation environment and a physical platform, as shown in Fig. 7 and Fig. 8, respectively. All system software was written using Python and

Robotic Operating System middleware [32]. The simulation was developed in Gazebo, an open-source software that is equipped with a physics engine, and component-wise emulates our physical platform. We used a custom magnetic dipole plugin that was previously developed by our group [28] for integrating magnetic wrenches with Gazebo's dynamics. The IM in the simulation is housed in a spherical shell. The shape is chosen to minimize effects of geometry on algorithm function. The IM's shell contains a tether whose primary purpose is to stabilize dynamics of the IM; however, an additional advantage of the tether is that it acts as a disturbance to IM motion that is likely to be more realistic than a simple untethered sphere. The physical platform has been previously developed for application in robotic-magnetic endoscopy [26], [28], [33]. The platform consists of a six DoF serial manipulator (RV6SDL, Mitsubishi, Inc., Japan) with an EM mounted at the end-effector and an IM housed in a tethered shell. Whereas the magnets in the simulation are modeled as perfect dipoles, in reality the EM is a cylindrical permanent magnet (N52 grade, 101.6 mm diameter and length, NdFeB, ND_N-10195, Magnetworld AG, Germany) that is magnetized in the axial direction and has a magnetic flux density of 1.48 T and the IM is another cylindrical permanent magnet (N52 grade, 11.11 mm diameter and length, NdFeB, D77-N52, K&J Magnetics, USA) with a magnetic flux density of 1.48 T. A force and torque sensor (Nano 17 SI-25-0.25, ATI Technologies) was used in force-control validation experiments. Data from this sensor was acquired using a 12 bit Analog-to-Digital converter that provided accuracy of 0.1 N and 0.5 $m \cdot Nm$. This sensor was mounted on, and manipulated by, a second serial manipulator (RV6SDL, Mitsubishi, Inc., Japan). The two manipulators were registered using a least-squares fitting [34].

The magnetic control solution to Eq. (14) is an EM motion, thus joint values of the serial manipulator must be computed to achieve the desired end-effector motion. To compute the necessary robot joint step, $\delta \mathbf{q}$ to achieve $\delta \mathbf{x}_e$, we use an actuation Jacobian, \mathbf{J}_A , defined in Eq. (16), where \mathbf{J}_R is the manipulator's geometric Jacobian. The Jacobian \mathbf{J}_A contains a redundancy in that a dipole can rotate about its magnetization axis without change in applied field owing to its field symmetry about its magnetization axis.

$$\delta \mathbf{x}_e = \begin{bmatrix} \mathbf{I} & \mathbf{0} \\ \mathbf{0} & \mathbf{S}(\hat{\mathbf{m}}_e)^T \end{bmatrix} \mathbf{J}_R \delta \mathbf{q} = \mathbf{J}_A \delta \mathbf{q} \quad (16)$$

The robot joint solution is shown in Eq. (17) where \mathbf{J}_A^+ denotes the *Moore-Penrose Pseudo Inverse* of the actuator Jacobian. Similar to β in Eq. (14), β_R is a user defined value that scales the projection of the gradient of an objective function, $h(\mathbf{q})$, onto the null space of \mathbf{J}_R . We chose $h(\mathbf{q})$ to represent the value of the manipulator's wrist, thus, after a threshold is reached, the manipulator uses available redundancy to prevent a collision between our EM's casing and the manipulator's link. The strategy is particular to our application and can be customized per future operator's needs.

$$\delta \mathbf{q} = \mathbf{J}_R^+ \delta \mathbf{x}_e + \beta_R (\mathbf{I} - \mathbf{J}_R^+ \mathbf{J}_R) \nabla_{\mathbf{q}} h(\mathbf{q}) \quad (17)$$

In the remainder of this section, we provide experimental demonstration of the functionality of our proposed method.

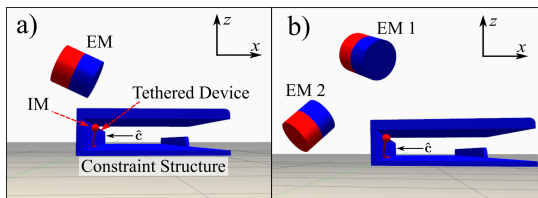


Fig. 7. Our Gazebo simulation environment with a) a single-EM environment and b) a double-EM environment. In all trials, a desired force was set in the $-x$ direction while motion was controlled in the y direction where a desired position was set.

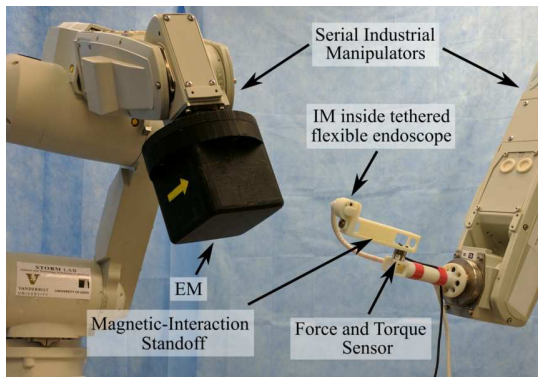


Fig. 8. The experimental platform that we used in physical experiments. A manipulator maneuvers an EM while another identical manipulator maneuvers an IM. The wrench applied on the IM is measured with a force and torque sensor.

We begin with a simulation study followed by experimental validation on a physical system.

B. Simulation Study

To evaluate our ability to algorithmically lower the value of g , and thus f_{c_a} and in turn f_c , when manipulating an IM, we conducted a series of simulation trials. The control was applied as stated in Eq. (14). The $\delta \mathbf{f}_{des}$ term was used for both position and force control as shown in Eq. (18) where \mathbf{e}_p and \mathbf{e}_f indicate position and force errors, respectively. Position is controlled in a motion direction that is orthogonal to $\hat{\mathbf{c}}$ and indicated by $\hat{\mathbf{p}}_m$. Both the contact force control and motion control directions are orthogonal to the vertical axis along which gravity is applied. The projection matrix that projects into this direction of motion is defined as $\mathbf{P}_m = \hat{\mathbf{p}}_m \hat{\mathbf{p}}_m^T$. Implementation of proportional-integral-derivative (PID) control is indicated via $pid()$. We conducted simulations with $\hat{\mathbf{c}}$ directed in the inertial $-x$ and y directions, referred to via $-\hat{\mathbf{x}}$ and $\hat{\mathbf{y}}$, respectively.

$$\delta \mathbf{f}_{des} = (\mathbf{I} - \mathbf{P}_m)pid(\mathbf{e}_f) + \mathbf{P}_m pid(\mathbf{e}_p) \quad (18)$$

We conducted one set of experiments using a Gaussian localization uncertainty of 10 mm and 10° and another with 15 mm and 15° ; the localization uncertainty was varied to observe whether algorithm performance was affected by noise magnitude. The localization uncertainty is applied in each pose component, *i.e.* position and orientation along all axes. These localization noise magnitudes were selected as they are near the upper boundary of uncertainty observed in physical

systems [9], [12], [16], [35]–[37]. Each set of experiments consisted of both “static” and “dynamic” trials. During the *static* trials, the IM is kept fully constrained while during *dynamic* trials, the IM and its tether are able to move freely and thus be subject to motion control in addition to force control. During *static* trials when $\hat{\mathbf{c}}$ was in the $-\hat{\mathbf{x}}$ direction, the IM’s heading was aligned with $\hat{\mathbf{c}}$, while during *static* trials when $\hat{\mathbf{c}}$ was in the $\hat{\mathbf{y}}$ direction, the IM’s heading was orthogonal to $\hat{\mathbf{c}}$, though still on the horizontal. This was done to evaluate the influence of various orientations.

We conducted the *static* and *dynamic* trials using both a single EM and two EMs, and conducted two sets of experiments for each combination of experimental parameters. These combinations can be visualized in the results Table II. Trials of “Set No.” 1 were subject to a desired force of 0.27 N in the direction of $\hat{\mathbf{c}}$ and 0.75 N in the vertical; this resulted in a desired force with a magnitude of 0.8 N and an orientation of 70° from $\hat{\mathbf{c}}$. Trials of “Set No.” 2 were subject to a desired force of 0.61 N in the direction of $\hat{\mathbf{c}}$ and 0.51 N in the vertical; this resulted in a desired force with a magnitude of 0.8 N and an orientation of 40° from $\hat{\mathbf{c}}$.

The dynamic trials of “Set No.” 1 resulted in the IM pressed against the contact-wall, as well as the upper-barrier, or ceiling, as shown in Fig 7. The dynamic trials of “Set No.” 2 resulted in the IM pressed against the contact wall, but floating in the vertical direction. Each “trial” consisted of five simulations run without the use of algorithm and five simulations with the algorithm. Each simulation ran for 80.0 s. Only the final 30.0 s of each simulation, the steady-state period, was post-processed as to avoid capturing data from the early, transient, period where magnets move to reduce force error and to reduce g . The homogeneous force solution that minimizes g was limited to a threshold magnitude after 35.0 s. A larger influence of the homogeneous component in the transient period allowed for the EM(s) to maneuver closer to a g minimum before the start of the steady-state period. We do not vary the magnitude of the particular solution between trials as modifying it would have an influence on force uncertainty and thus would not allow for a direct evaluation of the algorithm’s efficacy.

Results are shown in Table II (10 mm, 10° noise) and Table III (15 mm, 15° noise). The reported results in this table are the following: “ f_c err”: force error in $\hat{\mathbf{c}}$ from the desired, “ $g/|f_{c_a}|$ ”: the value of g normalized against force magnitude, CV_a , CV_t , and the ratios of CV_a and CV_t with and without the use of the algorithm. The values of CV_a were computed via dipole model using the noisy force estimate, *i.e.* what the algorithm “sees”, while the values of CV_t were computed via dipole model using the true IM pose. The final ratios explicitly show the factor of improvement in uncertainty when using our algorithm. The values reported here result from computation of the mean of the means of each simulation, *i.e.* the value reported as CV_a is the mean value of the CV_a ’s of each simulation and five simulations are conducted for each data point. A filter was used to smooth both EM commands and the computed gradient of g . We did not consider, nor compute the physics of, the interactions between the two actuating EMs. In a platform implementation, a component of actuation redundancy should be used to minimize the interaction force

between the EMs. We observed in our experiments that the EMs did tend to collide at times. Localization feedback was acquired at 100 Hz and was not filtered. The motion control in *dynamic* experiments was used to simply keep the IM in its initial position.

We observed that when the algorithm was used, the EMs changed orientation until a local minimum in g was reached. We found that the use of our algorithm robustly reduces uncertainty. The factor of improvement of CV_a was always above 1.0, and the factor of improvement of CV_t was typically at, or near, 1.0. The maximum factor of improvement of CV_t when using a single EM was 2.81 in *static* experiments and 1.69 in *dynamic* experiments. The maximum factor of improvement of CV_t during double-EM experiments was 1.65 in *static* experiments and 3.10 in *dynamic* experiments. We observe that uncertainty-improvement results for single-EM *static* trials were improved when the IM's heading was orthogonal to \hat{c} , as compared to when the heading was aligned with \hat{c} ; this suggests a varied ability for the EM to find various local minima in g . There was not a discernible effect in uncertainty reduction with varying levels of localization noise.

These results demonstrate that the algorithm robustly improves both the expected uncertainty, CV_a , and the true force uncertainty CV_t . It is noteworthy that the use of our algorithm also tended to reduce the error in f_c . Furthermore, we observed that the value of g/f_{c_a} was always reduced, demonstrating the controllability of ellipsoid size. We note that the improvement factor of CV_t was drastically smaller during double-magnet experiments of Set No. 2, and the error in f_c increased. This increase in uncertainty results from the IM's weight being nearly balanced by applied forces. The result differed significantly between cases of using the algorithm and not because when it was used, both EMs were near the workspace, *i.e.* near the IM and in proximity to each other. When the algorithm was not used, one EM drifted away from the workspace. As we are normalizing the gradient of g and capping the impact of the homogeneous solution, the two proximal EMs, which are moving with uncertainty, induce more uncertainty in applied force, which results in an increase in IM oscillation. This adverse effect would likely be improved by slowing the homogeneous solution and also would likely not be as evident in a physical system owing to the presence of environmental damping. We note that the factor of improvement of CV_a in these cases was greater than 1.0.

We found that one reason for limited controllability over the value of g is that the major axis of $\tilde{\mathbf{J}}_{F_i}$ tends to align with the magnetic force vector. The conclusion is based on a numerical simulation we conducted where 10,000 random EM poses were generated with a constant IM pose and the angle between the major ellipsoid axis of $\tilde{\mathbf{J}}_{F_i}$ and the magnetic force vector was recorded. The angle difference was found to be $22.9 \pm 16.6^\circ$. This simulation was repeated with a constraint that the $\hat{\mathbf{m}}_i$ aligns with the field of the EM where the result was $3.9 \pm 1.4^\circ$. These results suggest that a bias exists in the shape of the ellipsoid of $\tilde{\mathbf{J}}_{F_i}$, which is expected owing to the force being a direct result of field gradient. As a result of this, our algorithm typically had greater impact in experiments of Set. No. 1.

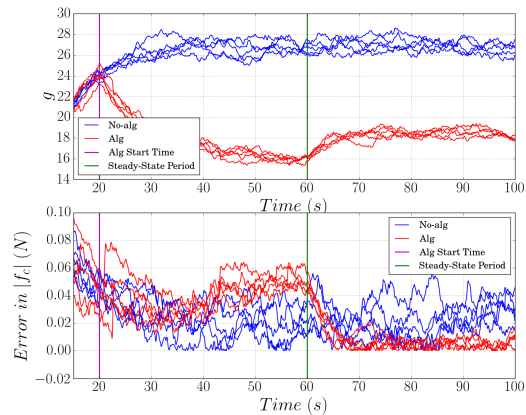


Fig. 9. The results of 5 static trials with and without the uncertainty-reducing algorithm where a 10 mm and 10° was applied. When using the algorithm, it was activated after 20 s. After 60 s, the homogeneous solution was scaled down, which we refer to as the start of the “steady-state period”. We do not alter the particular solution. In the top plot, the algorithm reduces the value of g . In the bottom plot, we show that the uncertainty is visibly lowered when the algorithm is in effect and its homogeneous twist that reduces g is scaled down. All data in these plots were filtered to improve visualization.

Finally, to demonstrate the algorithm's functionality in the transient during *static* experiments, we refer the reader to Fig. 9. Here, we followed a similar experiment protocol as shown in the results in Table II; however, the algorithm was activated after 20 s rather than immediately, to ensure that force error had reached a noisy steady state. The reduction in the value of g can be seen after 20 s, when the algorithm was activated. We observe that the force uncertainty drops during steady-state operation of the algorithm.

C. Evaluation on Physical System

Physical platform experiments were conducted to demonstrate the methodology on a real magnetic system. As we are not using an ideal dipole EM or IM for design purposes, we first begin by characterizing the sensitivity ellipsoids of our system in Section IV-C1. As the ability to draw conclusions and make algorithmic decisions based on sensitivity ellipsoid hinges on the validity of the dipole approximation, such characterization is recommended. We therefore conducted a series of experiments that show that the general behavior of ellipsoids in our physical system aligns with that which we expect from the linearized dipole model. We then discuss a set of experiments we conducted to evaluate the performance of our force-uncertainty-reducing algorithm in Section IV-C2. The experimental setup used for all platform experiments is shown in Fig. 8.

1) *Validation of Sensitivity Ellipsoids*: To validate the correspondence of ellipsoid shapes on our non-dipole platform with a dipole prediction, we utilize an EM that is moved by a serial manipulator and use a second serial manipulator to perturb the position and orientation of the IM. In general, force and torque can be applied in 3 DoF each, resulting in a 6 DoF task space. Only two torque DoFs are controllable owing to a dipole's symmetry. We are concerned with four primary

TABLE II
SIMULATION EXPERIMENT RESULTS. LOCALIZATION NOISE: 10 MM, 10°

Mode	EMs	\hat{c}	Set No.	No Algorithm				Algorithm				$\frac{CV_{a-no-alg}}{CV_{a-alg}}$	$\frac{CV_{t-no-alg}}{CV_{t-alg}}$
				f_c err (%)	$g/ f_{ca} $	CV_a	CV_t	f_c err (%)	$g/ f_{ca} $	CV_a	CV_t		
Static	1	$-\hat{x}$	1	6.2 ± 0.6	120.7	81.4	6.4	6.5 ± 0.7	105.2	74.9	5.8	1.09	1.10
			2	1.7 ± 0.3	57.7	32.7	2.0	2.2 ± 0.3	54.7	32.3	2.5	1.01	0.81
		\hat{y}	1	8.8 ± 2.5	107.9	78.3	6.0	3.2 ± 0.4	69.4	36.0	3.2	2.18	1.89
			2	4.1 ± 1.0	59.3	36.3	2.5	2.4 ± 0.1	55.3	33.2	2.8	1.10	0.88
	2	$-\hat{x}$	1	8.9 ± 1.1	122.8	80.8	10.4	5.3 ± 0.5	52.2	57.7	6.3	1.40	1.65
			2	3.4 ± 0.7	56.7	33.2	3.8	2.3 ± 0.4	28.6	22.1	2.6	1.50	1.47
Dynamic	1	$-\hat{x}$	1	18.1 ± 2.1	95.7	56.1	3.0	7.0 ± 1.2	81.9	49.3	1.8	1.14	1.62
			2	6.9 ± 0.7	55.8	29.7	1.2	7.3 ± 0.8	53.4	28.0	1.4	1.06	0.89
		\hat{y}	1	20.8 ± 1.1	94.3	55.0	2.7	7.4 ± 0.8	82.1	49.9	1.6	1.10	1.69
			2	7.8 ± 1.6	55.4	29.8	1.3	7.7 ± 1.3	52.8	28.3	1.2	1.05	1.07
	2	$-\hat{x}$	1	16.1 ± 1.8	97.0	56.9	3.63	6.6 ± 1.7	25.1	24.6	1.2	2.31	3.10
			2	7.6 ± 0.5	55.3	30.2	1.8	94.2 ± 71.9	34.4	24.9	10.6	1.21	0.17
		\hat{y}	1	17.0 ± 0.7	95.4	57.8	3.2	6.3 ± 2.6	27.6	26.4	2.1	2.19	1.52
			2	7.3 ± 1.5	54.9	29.9	1.8	218.0 ± 100.9	44.2	27.6	13.0	1.09	0.14

TABLE III
SIMULATION EXPERIMENT RESULTS. LOCALIZATION NOISE: 15 MM, 15°

Mode	EMs	\hat{c}	Set No.	No Algorithm				Algorithm				$\frac{CV_{a-no-alg}}{CV_{a-alg}}$	$\frac{CV_{t-no-alg}}{CV_{t-alg}}$
				f_c err (%)	$g/ f_{ca} $	CV_a	CV_t	f_c err (%)	$g/ f_{ca} $	CV_a	CV_t		
Static	1	$-\hat{x}$	1	18.2 ± 3.0	138.3	143.4	10.2	14.7 ± 3.2	114.5	124.8	9.5	1.15	1.07
			2	3.4 ± 0.8	59.2	51.7	3.2	3.3 ± 0.5	57.1	51.0	3.2	1.01	1.01
		\hat{y}	1	18.6 ± 4.5	108.3	126.7	11.0	5.1 ± 1.2	73.0	62.1	3.9	2.04	2.81
			2	9.9 ± 1.9	59.9	60.7	4.3	8.0 ± 3.3	58.0	57.1	4.3	1.06	1.01
	2	$-\hat{x}$	1	15.3 ± 2.7	139.5	147.3	13.0	13.5 ± 4.1	86.6	107.5	11.0	1.37	1.18
			2	4.6 ± 1.0	59.9	53.1	4.9	4.0 ± 0.5	39.1	38.4	4.7	1.38	1.05
	\hat{y}	1	8.8 ± 1.4	126.0	119.3	9.8	10.5 ± 1.9	39.4	91.7	8.3	1.30	1.18	
		2	5.9 ± 1.6	65.4	58.1	6.2	6.5 ± 0.9	14.2	37.9	3.7	1.53	1.65	
Dynamic	1	$-\hat{x}$	1	30.9 ± 3.0	98.9	88.1	2.0	15.3 ± 3.4	87.0	81.4	1.5	1.08	1.33
			2	18.8 ± 1.0	59.1	47.7	1.7	15.0 ± 1.2	55.3	46.6	1.8	1.02	0.95
		\hat{y}	1	33.4 ± 4.0	98.1	82.0	2.2	18.5 ± 3.1	87.3	79.6	1.7	1.03	1.32
			2	21.2 ± 2.3	58.3	48.8	1.9	18.4 ± 1.7	55.3	46.0	1.8	1.06	1.03
	2	$-\hat{x}$	1	27.3 ± 3.7	103.6	90.9	3.9	8.2 ± 3.6	24.75	41.75	2.4	2.18	1.63
			2	17.8 ± 1.7	58.4	48.0	2.1	35.5 ± 29.6	30.7	34.6	8.3	1.39	0.25
	\hat{y}	1	28.8 ± 2.6	99.8	89.2	3.9	12.5 ± 2.0	26.4	44.4	1.7	2.01	2.28	
		2	17.1 ± 2.3	58.4	48.3	2.2	28.8 ± 9.1	29.4	30.0	10.3	1.61	0.21	

Jacobians that were defined in Eq. (6): \mathbf{J}_{Fp_i} , $\tilde{\mathbf{J}}_{F\omega_i}$, \mathbf{J}_{Tp_i} , and $\tilde{\mathbf{J}}_{T\omega_i}$, each of which are $\in \mathbb{R}^{3 \times 3}$. As we wish to convey the similarity in ellipsoid shape, it is most intuitive to visualize the ellipsoids in 2D. For each Jacobian, nine 2 DoF combinations exist, thus, the reader will see nine individual plots for each Jacobian that was validated.

Discrete points that form the sensitivity ellipsoids are experimentally recorded by perturbing the pose of the IM in planes e.g. moving the IM in a circle on the XY plane, then XZ plane, then YZ plane, and repeating for angular DoFs. As the IM is mounted on a force and torque sensor, force and torque are recorded at each of these poses. We chose to discretize each circle in 12 data points. At each of these 12 points, 2000 force and torque readings were collected. As many of the perturbations were within the sensitivity of the force and torque sensor, the large number of data points allowed for a more accurate mean reading. Finally, the resultant ellipsoids of force and torque perturbations were plotted along with the predicted dipole-dipole Jacobian value as well as the discrete theoretical expected result obtained from dipole force and torque equations. This theoretical discrete expected result was computed by gathering data at each discrete point as

traveled by the IM; however, instead of a measurement, it is the force and torque as estimated via dipole-dipole model. This computed result is shown to visualize potential losses of Jacobian linearity. Given that the dipole force and torque estimates may have slight inaccuracies, we are more interested in the general behavior of a Jacobian; thus, we accept improper scaling of an ellipsoid, or minor deviations from the expected shape. We conducted multiple sets of experiments and show the results of one of these in Fig. 10.

We evaluated the ellipsoids' correctness by computing the measured and dipole-predicted major to minor axis length ratio, as well as the angle tilt of the ellipsoid. For the data shown in Fig. 10, we found the ellipsoid axis ratio to be have an error of $27.0 \pm 25.7\%$ and an ellipse tilt error of $10.0 \pm 17.8^\circ$ (36 ellipsoids). Results of 8 tests were recorded, 2 of which were marked as outliers. The results of the 6 tests were: an ellipse ratio error of $47.7 \pm 79.9\%$ and an ellipse tilt error of $13.5 \pm 20.5^\circ$. When processing the result for all 8 trials, including the outliers, the results were $86.1 \pm 204.4\%$ and $13.5 \pm 19.6^\circ$ for ellipse ratio error and ellipse tilt error, respectively. The high errors are likely attributed to the greater impact of sensor noise and robot registration errors

in instances where the magnetic Jacobian is ill-conditioned *i.e.* the Jacobian's ellipsoids are thinner in certain DoFs. We emphasize that the correctness of sensitivity ellipsoid direction compared to magnitude is more important in our application as this direction is used by our algorithm to dictate EM motions. As the measured behavior of the ellipsoids is, in general, consistent with the linearized dipole model, only one set of results is shown. We conclude that on our physical system, we can use the dipole model to draw conclusions regarding sensitivity. Any errors that may exist in the ellipsoid assumption will adversely affect performance.

2) *Force Control Algorithm Evaluation:* We experimentally validated the force control algorithm's function on our physical platform by using an external sensor measurement to confirm that force uncertainty was reduced. These experiments were conducted while keeping the IM in a fixed pose as shown in Fig. 8. Owing to the presence of two serial robots in close proximity, the experimental workspace was small. Given an initial condition of magnet positions, the use of our uncertainty-reducing algorithm results in a new EM pose that is unknown at the start of the experiment; this presents a path-planning problem for collision avoidance. In this work, we avoided the development of a path-planning algorithm, and instead conducted a brute-force numerical simulation that tests initial experimental parameters and determines if the EM is likely to approach an undesirable configuration. Given a set of acceptable conditions, *i.e.* that would not result in robot collision, we chose conditions that were expected to reduce the size of g more significantly, and thus be more likely to reduce CV_t by a larger amount. We note that such a search was not done in any simulation trials. Whereas we wished to demonstrate how much CV_t can be affected by applying our methodology, we emphasize that the system can use the force uncertainty reducing algorithm constantly; the system will take advantage of the null-space reduction of g when possible.

In these experiments, we commanded a desired force, based on a PID control on force error, to apply on the IM using the relations shown in Eq. (14) and Eq. (19).

$$\delta \mathbf{f}_{des} = pid(\mathbf{e}_f) \quad (19)$$

Similar to the protocol for simulations, we conducted eight experiments which each consisted of five trials without the algorithm, and five trials with the algorithm. We recorded data for 80 s and analyzed the final 30 s to capture steady-state behavior. A trial period of 80 s allowed the system to reach a steady-state point in any attempted experiment configuration. The joint values sent to the manipulator were filtered to avoid shaking of the robot. As in some simulations, during all experiments, a Gaussian localization uncertainty was set to 15 mm and 15°. Localization feedback was acquired at approximately 100 Hz and was not filtered. The true value of f_c was measured using a force and torque sensor mounted on the end-effector of a second serial manipulator (Fig. 8).

The experimental results are reported in Table IV. The reported values were computed in the same manner as they were in simulation trials; however, the value of CV_t here was computed using the external sensor, rather than a dipole-model estimate. The outcome of our results analysis is the mean value

of g that is normalized by dividing by the mean $|f_{c_a}|$, as well as CV_a that was defined in Eq. (11), and CV_t that was defined in Eq. (12). The true value of contact force, f_c , was obtained from sensor measurements. We found that, by using our algorithm, we were able to reduce CV_a by a factor of up to 4.6, and reduce CV_t by a factor of up to 2.5 (trial 4).

V. DISCUSSION

We have demonstrated the functionality of our force uncertainty reducing algorithm in both simulations and platform experiments. We found that our algorithm was able to reduce force uncertainty in the majority of simulations and all platform experiments. We evaluated the algorithm in the case of using a single EM as well as using two EMs. We demonstrated functionality in two directions as well as with two various levels of localization noise. We conducted all simulations in both a static manner, where the IM was fixed in space, as well as in a dynamic manner, where the IM was free to move in response to environmental forces. Our algorithm reduced force uncertainty in both static and dynamic experiments. Furthermore, the methodology applied in this manuscript may be improved by differentiating magnet heading in an \mathbb{S}^2 manifold, as the magnetic strength of a permanent magnet is constant. Furthermore, we note that a further improvement to the proposed method may include a consideration for the sensitivity of actuation Jacobians, *e.g.* $\mathbf{J}_{F_{e_k}}$ (Eq. (7)), to localization noise and, in turn, the implications of their ellipsoid shapes.

In this work, we did not focus on optimizing force control accuracy *i.e.* ensuring that the obtained force was precisely what was desired, for two reasons: (1) on our platform, the magnets are not ideal dipoles and thus any measured force error is attributed to both robot registration error as well as imperfect field modeling and (2) we found that the same control methodology cannot be applied for all experiments *i.e.* control gains must be adjusted based on amount of force and amount of localization noise. To address (1), a future researcher can use spherical magnets or implement more accurate field models such as the current model [27]. Works in robotic capsule endoscopy have implemented such models previously [38]. To address (2), an adaptive controller is likely a proper solution assuming that the field modelling is accurate. We specifically opted to not adjust control parameters between trials as to minimize the number of variables in the analysis. To compensate for this effect, we presented our results in a normalized manner with respect to force magnitude.

This work is relevant for groups working with magnetic manipulation of *in-vivo* devices whether they be untethered or partially constrained by a catheter or continuum robot. The methods were developed for permanent magnet systems where the IM is a single dipole, but can be extended to cases where multiple IMs are used or if the controlled device is composed of a sphere of soft-magnetic material such that effects of shape on magnetization are negligible [39], [40]. In such case, the actuation system would gain torque redundancy as the soft-magnetic material would be less likely to align with the external field. Our methods can also be extended

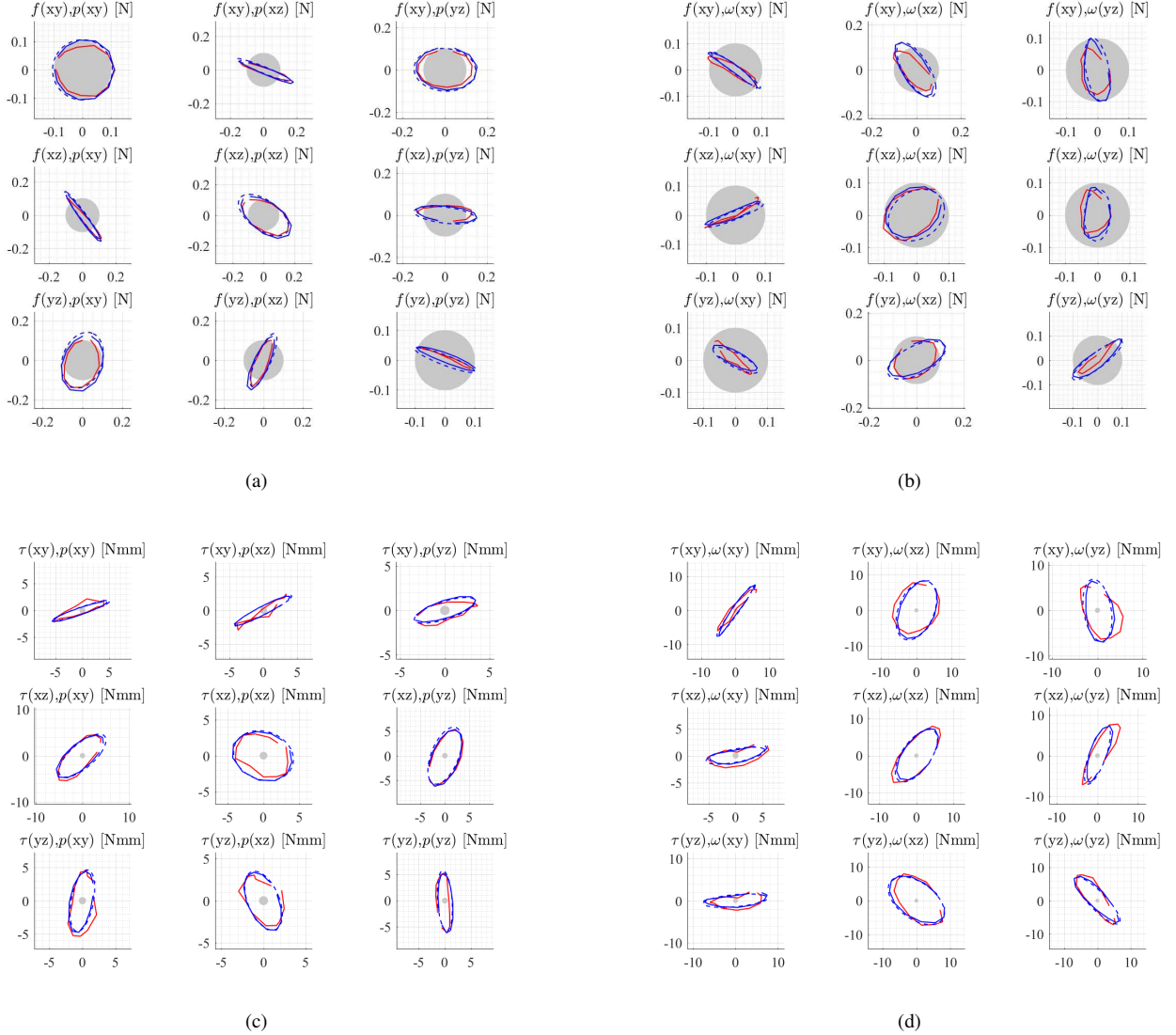


Fig. 10. Results of a pose perturbation experiment showing the consistency between theoretical and observed behavior of the $\tilde{\mathbf{J}}_i$ Jacobian. The configuration of the magnets is arbitrary: $\mathbf{p} = [0.125, -0.069, -0.065]$, $\hat{\mathbf{m}}_i = [0.422, -0.887, -0.187]$, and $\hat{\mathbf{m}}_e = [-0.909, 0.415, 0.044]$. The magnets were separated by 16 cm, with respective nominal dipole force and torque magnitudes of 1.0 N and 37 N-mm. Here, the red line represents the experimental result, the solid blue line represents the discrete theoretical result, and the dashed blue line represents the theoretical Jacobian prediction. The gray circle indicates the sensors sensitivity. Shown are the experimental and theoretical results for the Jacobians: (a) $\mathbf{J}_{F p_i}$, (b) $\tilde{\mathbf{J}}_{F \omega_i}$, (c) $\mathbf{J}_{T p_i}$, and (d) $\tilde{\mathbf{J}}_{T \omega_i}$

to electromagnetic actuation systems by adding derivative relations between coil currents. As four coils are needed for a force control task and eight coils are needed for a force-and-torque control task, torque redundancy can be used for implementing our proposed algorithm [41]. Our methodology was evaluated on a cm-scale system but can be applied for control of robots in smaller scales where precision of motion is especially necessary. Finally, this work gives insight into the use of manipulability ellipsoids for magnetic actuation, as is commonly done for rigid-link manipulators.

VI. CONCLUSION

In this work, we used a sensitivity ellipsoid analysis of a magnetic actuation Jacobian to improve the uncertainty in applied force in the presence of localization noise. Our method

relies on defining a direction during a force control task in which the precision of force application is favored. By manipulating the configuration of the EM in the differential force nullspace, our proposed algorithm minimizes the shape of a sensitivity ellipsoid in the direction of desired force precision improvement. We demonstrated that this method decreases the uncertainty in applied force both in simulation and physical experiments. In simulation experiments, an IM that was embedded in a tethered shell was commanded to a force control task in cases where the IM was fixed in space, as well as free to rotate. The latter experiments demonstrated that although the IM was rotated owing to the algorithm acting in the force nullspace and thus applying varying torques, the force uncertainty was still decreased. We conducted physical experiments on our platform intended for magnetic endoscopy

TABLE IV
PLATFORM EXPERIMENT RESULTS

Trial No.	Des. Force (N)	No Algorithm			Algorithm			$\frac{CV_{no-alg}}{CV_{alg}}$	$\frac{CV_{no-alg}}{CV_{alg}}$
		$g/ f_{ca} $	CV_a	CV_t	$g/ f_{ca} $	CV_a	CV_t		
1	[-0.05, -0.16, 0.47]	306.6	346.3	41.0	62.0	123.1	18.6	2.81	2.20
2	[-0.04, -0.31, 0.39]	395.4	384.5	35.4	288.1	295.5	32.7	1.30	1.08
3	[-0.08, -0.27, 0.41]	212.9	224.1	28.4	63.6	95.9	12.3	2.34	2.31
4	[-0.07, -0.07, 0.49]	238.3	287.0	45.5	54.9	86.0	18.2	3.34	2.50
5	[-0.12, -0.39, 0.29]	168.6	171.6	17.9	61.7	16.6	9.3	2.24	1.93
6	[-0.10, -0.11, 0.48]	154.6	174.2	20.5	63.3	89.2	11.5	1.95	1.79
7	[-0.11, -0.34, 0.34]	158.3	153.0	17.7	72.0	67.7	10.1	2.26	1.66
8	[-0.09, -0.30, 0.39]	211.1	246.4	27.9	53.7	53.5	11.4	4.61	2.45

and demonstrated a decrease in force uncertainty when the IM was constrained. Whereas force control is useful in and of itself, it is the intrinsic method for actuating magnetically controlled robots as no rigid coupling exists between an actuator and an end-effector. This method may be applied in systems with mechanical constraints, such as magnetically guided catheters or continuum robots, where the orientation of a guiding IM is partially constrained. Increasing accuracy of the force applied will affect the motion of magnetic robots to a degree that will vary based on the magnitude of localization uncertainty.

ACKNOWLEDGMENT

Any opinions, findings, conclusions, or recommendations expressed in this material are those of the authors and do not necessarily reflect the views of the National Institutes of Health, the National Science Foundation, the Royal Society, the Engineering and Physical Sciences Research Council, or the Italian Ministry of Health.

REFERENCES

- [1] G. Gillies, R. Ritter, W. Broaddus, M. Grady, M. Howard III, and R. McNeil, "Magnetic manipulation instrumentation for medical physics research," *Review of Scientific Instruments*, vol. 65, no. 3, pp. 533–562, 1994.
- [2] P. R. Slawinski, K. L. Obstein, and P. Valdastrì, "Capsule endoscopy of the future: Whats on the horizon?" *World Journal of Gastroenterology: WJG*, vol. 21, no. 37, p. 10528, 2015.
- [3] N. Simaan, R. M. Yasin, and L. Wang, "Medical technologies and challenges of robot-assisted minimally invasive intervention and diagnostics," *Annual Review of Control, Robotics, and Autonomous Systems*, vol. 1, no. 1, pp. 465–490, 2018. [Online]. Available: <https://doi.org/10.1146/annurev-control-060117-104956>
- [4] H. Ren and J. Sun, *Electromagnetic Actuation and Sensing in Medical Robotics*. Springer, 2018.
- [5] L. J. Sliker and G. Ciuti, "Flexible and capsule endoscopy for screening, diagnosis and treatment," *Expert Review of Medical Devices*, vol. 11, no. 6, pp. 649–666, 2014.
- [6] X.-Z. Chen, M. Hoop, F. Mushtaq, E. Siringil, C. Hu, B. J. Nelson, and S. Pané, "Recent developments in magnetically driven micro-and nanorobots," *Applied Materials Today*, vol. 9, pp. 37–48, 2017.
- [7] A. W. Mahoney and J. J. Abbott, "Five-degree-of-freedom manipulation of an untethered magnetic device in fluid using a single permanent magnet with application in stomach capsule endoscopy," *The International Journal of Robotics Research*, vol. 35, no. 1-3, pp. 129–147, 2016.
- [8] K. M. Popek, T. Hermans, and J. J. Abbott, "First demonstration of simultaneous localization and propulsion of a magnetic capsule in a lumen using a single rotating magnet," in *Robotics and Automation (ICRA), 2017 IEEE International Conference on*. IEEE, 2017, pp. 1154–1160.
- [9] A. Z. Taddese, P. R. Slawinski, M. Pirota, E. De Momi, K. L. Obstein, and P. Valdastrì, "Enhanced real-time pose estimation for closed loop robotic manipulation of magnetically actuated capsule endoscopes," *The International Journal of Robotics Research*, vol. 37, no. 8, pp. 890–911, 2018.
- [10] J. Edelmann, A. J. Petruska, and B. J. Nelson, "Estimation-based control of a magnetic endoscope without device localization," *Journal of Medical Robotics Research*, vol. 3, no. 01, p. 1850002, 2018.
- [11] M. P. Kummer, J. J. Abbott, B. E. Kratochvil, R. Borer, A. Sengul, and B. J. Nelson, "Octomag: An electromagnetic system for 5-dof wireless micromanipulation," *IEEE Transactions on Robotics*, vol. 26, no. 6, pp. 1006–1017, 2010.
- [12] R. Chandra, A. J. Johansson, M. Gustafsson, and F. Tufvesson, "A microwave imaging-based technique to localize an in-body rf source for biomedical applications," *IEEE Transactions on Biomedical Engineering*, vol. 62, no. 5, pp. 1231–1241, 2015.
- [13] K. Pahlavan, G. Bao, Y. Ye, S. Makarov, U. Khan, P. Swar, D. Cave, A. Karellas, P. Krishnamurthy, and K. Sayrafiyan, "Rf localization for wireless video capsule endoscopy," *International Journal of Wireless Information Networks*, vol. 19, no. 4, pp. 326–340, 2012.
- [14] M. Fluckiger and B. J. Nelson, "Ultrasound emitter localization in heterogeneous media," in *Engineering in Medicine and Biology Society, 2007. EMBS 2007. 29th Annual International Conference of the IEEE*. IEEE, 2007, pp. 2867–2870.
- [15] T. D. Than, G. Alici, H. Zhou, S. Harvey, and W. Li, "Enhanced localization of robotic capsule endoscopes using positron emission markers and rigid-body transformation," *IEEE Transactions on Systems, Man, and Cybernetics: Systems*, vol. PP, no. 99, pp. 1–15, 2017.
- [16] C. Di Natali, M. Beccani, N. Simaan, and P. Valdastrì, "Jacobian-based iterative method for magnetic localization in robotic capsule endoscopy," *IEEE Transactions on Robotics*, vol. 32, no. 2, pp. 327–338, 2016.
- [17] D. Son, S. Yim, and M. Sitti, "A 5-d localization method for a magnetically manipulated untethered robot using a 2-d array of hall-effect sensors," *IEEE/ASME Transactions on Mechatronics*, vol. 21, no. 2, pp. 708–716, 2016.
- [18] X. Guo, C. Wang, and R. Yan, "An electromagnetic localization method for medical micro-devices based on adaptive particle swarm optimization with neighborhood search," *Measurement*, vol. 44, no. 5, pp. 852–858, 2011.
- [19] T. Yoshikawa, "Manipulability of robotic mechanisms," *The international journal of Robotics Research*, vol. 4, no. 2, pp. 3–9, 1985.
- [20] X. Li, X. Ding, and G. S. Chirikjian, "Analysis of angular-error uncertainty in planar multiple-loop structures with joint clearances," *Mechanism and Machine Theory*, vol. 91, pp. 69–85, 2015.
- [21] P. Chiacchio, S. Chiaverini, L. Sciavicco, and B. Siciliano, "Global task space manipulability ellipsoids for multiple-arm systems," *IEEE Transactions on Robotics and Automation*, vol. 7, no. 5, pp. 678–685, 1991.
- [22] A. W. Mahoney and J. J. Abbott, "Control of untethered magnetically actuated tools with localization uncertainty using a rotating permanent magnet," in *2012 4th IEEE RAS & EMBS International Conference on Biomedical Robotics and Biomechatronics (BioRob)*. IEEE, 2012, pp. 1632–1637.
- [23] T. Yoshikawa, "Analysis and control of robot manipulators with redundancy," in *Robotics research: the first international symposium*. MIT Press Cambridge, MA, USA, 1984, pp. 735–747.

- [24] J. Sikorski, I. Dawson, A. Denasi, E. E. Hekman, and S. Misra, "Introducing bigmaga novel system for 3d magnetic actuation of flexible surgical manipulators," in *Robotics and Automation (ICRA), 2017 IEEE International Conference on*. IEEE, 2017, pp. 3594–3599.
- [25] A. J. Petruska and J. J. Abbott, "Optimal permanent-magnet geometries for dipole field approximation," *IEEE transactions on magnetics*, vol. 49, no. 2, pp. 811–819, 2013.
- [26] P. R. Slawinski, A. Z. Taddese, K. B. Musto, K. L. Obstein, and P. Valdastri, "Autonomous retroflexion of a magnetic flexible endoscope," *IEEE Robotics and Automation Letters*, vol. 2, no. 3, pp. 1352–1359, 2017.
- [27] E. P. Furlani, *Permanent magnet and electromechanical devices: materials, analysis, and applications*. Academic press, 2001.
- [28] A. Z. Taddese, P. R. Slawinski, K. L. Obstein, and P. Valdastri, "Closed loop control of a tethered magnetic capsule endoscope," in *Proc. 2016 Robotics: Sci. and Syst.*, Ann Arbor, Michigan, USA, 2016.
- [29] Y. Nakamura, *Advanced robotics: redundancy and optimization*. Addison-Wesley Longman Publishing Co., Inc., 1990.
- [30] L. Sciavicco and B. Siciliano, *Modelling and control of robot manipulators*. Springer Science & Business Media, 2012.
- [31] A. Liegeois, "Automatic supervisory control of the configuration and behavior of multibody mechanisms," *IEEE transactions on systems, man, and cybernetics*, vol. 7, no. 12, pp. 868–871, 1977.
- [32] M. Quigley, K. Conley, B. Gerkey, J. Faust, T. Foote, J. Leibs, R. Wheeler, and A. Y. Ng, "Ros: an open-source robot operating system," in *ICRA workshop on open source software*, vol. 3, no. 3.2. Kobe, 2009, p. 5.
- [33] A. Z. Taddese, P. R. Slawinski, K. L. Obstein, and P. Valdastri, "Non-holonomic Closed-loop Velocity Control of a Soft-tethered Magnetic Endoscope," in *IEEE/RSJ Int. Conf. Intell. Robot. Syst. (IROS 2016)*, Daejeon, South Korea, 2016.
- [34] K. S. Arun, T. S. Huang, and S. D. Blostein, "Least-squares fitting of two 3-d point sets," *IEEE Transactions on pattern analysis and machine intelligence*, no. 5, pp. 698–700, 1987.
- [35] M. Salerno, G. Ciuti, G. Lucarini, R. Rizzo, P. Valdastri, A. Menciassi, A. Landi, and P. Dario, "A discrete-time localization method for capsule endoscopy based on on-board magnetic sensing," *Measurement Science and Technology*, vol. 23, no. 1, p. 015701, jan 2012.
- [36] C. Di Natali, M. Beccani, and P. Valdastri, "Real-time pose detection for magnetic medical devices," *IEEE Trans. Magn.*, vol. 49, no. 7, pp. 3524–3527, 2013.
- [37] K. M. Popek, T. Schmid, and J. J. Abbott, "Six-Degree-of-Freedom Localization of an Untethered Magnetic Capsule Using a Single Rotating Magnetic Dipole," *IEEE Robotics and Automation Letters*, vol. 2, no. 1, pp. 305–312, jan 2017.
- [38] M. Salerno, R. Rizzo, E. Sinibaldi, and A. Menciassi, "Force calculation for localized magnetic driven capsule endoscopes," in *IEEE International Conference on Robotics and Automation*, 2013, pp. 5354–5359.
- [39] O. Ergeneman, G. Dogangil, M. P. Kummer, J. J. Abbott, M. K. Nazeeruddin, and B. J. Nelson, "A magnetically controlled wireless optical oxygen sensor for intraocular measurements," *IEEE Sensors Journal*, vol. 8, no. 1, pp. 29–37, 2008.
- [40] J. J. Abbott, O. Ergeneman, M. P. Kummer, A. M. Hirt, and B. J. Nelson, "Modeling magnetic torque and force for controlled manipulation of soft-magnetic bodies," *IEEE Transactions on Robotics*, vol. 23, no. 6, pp. 1247–1252, 2007.
- [41] A. J. Petruska and B. J. Nelson, "Minimum bounds on the number of electromagnets required for remote magnetic manipulation," *IEEE Transactions on Robotics*, vol. 31, no. 3, pp. 714–722, 2015.



Piotr R. Slawinski (S'15) received his B.S. degree in mechanical engineering from the University of Nebraska-Lincoln in 2013 and his M.S. degree in mechanical engineering from Vanderbilt University in 2018. He is currently pursuing the Ph.D. degree in mechanical engineering at Vanderbilt University, Nashville, TN, USA. His research focus is on the magnetic actuation of medical robots. Mr. Slawinski was a Graduate Research Fellow of the National Science Foundation.



Nabil Simaan (M'04, SM'13) received his Ph.D. degree in mechanical engineering from the Technion-Israel Institute of Technology, Haifa, Israel, in 2002. During 2003, he was a Postdoctoral Research Scientist at Johns Hopkins University National Science Foundation (NSF) Engineering Research Center for Computer-Integrated Surgical Systems and Technology (ERC-CISST). In 2005, he joined Columbia University, New York, NY, as an Assistant Professor of mechanical engineering and the Director of the Advanced Robotics and Mechanisms Applications (ARMA) Laboratory. In 2009 he received the NSF Career award for young investigators to design new algorithms and robots for safe interaction with the anatomy. In Fall 2010 he joined Vanderbilt University as an Associate Professor, Nashville, TN. His research interests include continuum robots, parallel mechanisms, human-robot physical interaction and surgical robotics.



Addisu Z. Taddese received his Ph.D degree in electrical engineering from Vanderbilt University, Nashville, TN, USA in 2018.

His research focused on magnetically actuated capsules endoscopy. He is currently a software engineer at Open Robotics, Mountain View, CA.

Dr. Taddese was a Graduate Fellow of the National Science Foundation.



Keith L. Obstein earned his B.S. from Johns Hopkins University Whiting School of Engineering (Baltimore, MD), M.D. from Northwestern University (Chicago, IL), and M.P.H. from Harvard University School of Public Health (Boston, MA). He completed Internal Medicine residency at the Hospital of the University of Pennsylvania (Philadelphia, PA) and Gastroenterology (GI) fellowship at the Brigham and Womens Hospital (Boston, MA).

Currently, he is an Associate Professor of Medicine and of Mechanical Engineering at Vanderbilt University (Nashville, TN). He is also the Program Director of the Vanderbilt GI Fellowship training program and Director of the Science and Technology Of Robotics in Medicine (STORM) Lab USA at Vanderbilt. He is an active clinician and conducts research in the areas of New Technologies, Robotics, Device Development, Endoscopic Training, and Healthcare Quality Improvement.

Dr. Obstein is a Fellow of the American Society for Gastrointestinal Endoscopy (FASGE), a Fellow of the American College of Gastroenterology (FACG), and is board certified in gastroenterology. He serves on the ASGE Recognized Industry Associate (ARIA) task force, the ASGE member engagement and diversity committee, the ACG public relations committee, and is the Continuing Medical Education (CME) special section editor of the journal *Gastroenterology*.



Pietro Valdastri (M'05, SM'13) received the Ph.D. degree in Robotics from Scuola Superiore Sant'Anna (SSSA), Italy, in 2006. He was Assistant Professor at the Institute of BioRobotics, SSSA (2008-2010) and in the Department of Mechanical Engineering, Vanderbilt University (2011 - 2016). Since 2016, he is Professor and Chair in Robotics and Autonomous Systems at the University of Leeds, UK, and Director of the STORM Lab UK. His research interests are in robotic endoscopy and surgery, with a focus on frugal innovation and magnetic manipulation. In

2015, he received the NSF Career award to study and design capsule robots for medical applications, while in 2019, he received an ERC Consolidator Grant to investigate magnetic tentacles for surgical applications.